Wind and Structures, *Vol. 29, No. 1 (2019) 55-64*
DOI: https://doi.org/10.12989/was.2019.29.1.055

Wakes of two inline cylinders at a low Reynolds number

Farhan Zafar[1], Md. Mahbub Alam[*1], Zaka Muhammad[1] and Md. Islam[2]

[1]*Institute for Turbulence-Noise-Vibration Interaction and Control*
Harbin Institute of Technology (Shenzhen),Shenzhen 518055, China
[2]*Department of Mechanical Engineering, Khalifa University of Science and Technology,*
P.O. Box 2533, Abu Dhabi, United Arab Emirates

(Received November 14, 2017, Revised December 27, 2018, Accepted January 13, 2019)

Abstract. The effect of vortex impingement on the fluid dynamics around a cylinder submerged in the wake of another of different diameters is numerically investigated at a Reynolds number Re = 200. While the diameter (D) of the downstream cylinder is fixed, impinging vortices are produced from the upstream cylinder diameter (d) varied as d/D = 0.24, 0.4, 0.6, 0.8 and 1.0, with a spacing ratio L = 5.5d, where L is the distance between the center of the upstream cylinder to the front stagnation point of the downstream cylinder. Two-dimensional simulations are carried out using the finite volume method. Fluid forces acting on the two cylinders are correlated with impinging vortices, vortex shedding, and wake structure. Different facets of wake formation, wake structure, and flow separation and their connections to fluid forces are discussed.

Keywords: complex terrain; typhoon wind field; CFD simulation; surface roughness length; topography

1. Introduction

Flow around a circular cylinder submerged in a wake has potential applications in various engineering fields, such as offshore piggyback pipelines, shell and tube bundles heat exchangers, cooling system for electronic components, turbine blades, etc. The tandem configuration of two cylinders is classic for analyzing the complex flow features around multiple cylindrical structures. Spacing ratio L/d is a governing parameter defining the flow around two tandem cylinders, where L is the distance from the upstream cylinder center to the front stagnation point of the downstream cylinder, and d is the upstream cylinder diameter. Here we define the downstream cylinder diameter as D. For d/D = 1.0, with increasing L/d, the flow around two tandem cylinders changes as: **overshoot flow** ($0.5 < L/d < 0.7$–1.3) where the upstream-cylinder shear layers shed vortices behind the downstream cylinder without reattaching on it; **reattachment flow** (0.7–$1.3 < L/d < 2.9$–3.3) where the upstream-cylinder shear layers reattach on the downstream cylinder; and **coshedding flow** ($L/d > 2.9$–3.5) where the upstream-cylinder shear layers roll in the gap between the cylinders without reattachment (Zdravkovich 1987, Alam *et al.* 2003a). A bistable nature of the flow emerges for a small range of L/d at the boundary between the reattachment and coshedding flow regimes, where the reattachment and coshedding flows intermittently switch from one to the other. This range of L/d is called bistable flow regime (Alam 2014). The boundaries between the flow regimes are contingent on the freestream turbulent intensity and Reynolds number $Re = U_\infty D/\nu$, where U_∞ is the free velocity and ν is the kinematic viscosity of fluid (Sakamoto and Haniu 1988, Alam 2014).

Naturally, diameters of cylindrical structures in a group are not always identical but different. Attention has thus been paid to assimilate the effect of $d/D > 1.0$ or $d/D < 1.0$ on aerodynamic forces and flow structures around the cylinders. Igarashi (1982) at $1.3 \times 10^4 \leq Re \leq 5.8 \times 10^4$ identified overshoot, reattachment, bistable and coshedding flow patterns for d/D = 1.47 in a similar fashion to those for d/D = 1.0. The L/d ranges for different flow regimes are, however, distinct from those for d/D = 1.0, with the L/d range of the bistable flow being significantly smaller for d/D = 1.47. Sakamoto and Haniu (1994) utilized a small cylinder of diameter d around the main circular cylinder of diameter D to suppress aerodynamic forces at $Re = 6.5 \times 10^4$ by controlling the boundary layer and shear layer separated from the surface of the main cylinder. They were able to achieve a maximum reduction of 50% in time-mean drag $\bar{C}_D$, 85% in fluctuating lift and drag for d/D = 0.06 when the control cylinder position was at 60^o and 120^o measured from the nominal front stagnation point. A control cylinder or a control flat plate has been implemented in some studies to suppress the fluid forces on a single circular or square cylinder and on multiple cylinders (Igarashi 1997, Prasad and Williamson 1997, Bouak and Lemay 1998, Alam *et al.* 2002, Tsutsui and Igarashi 2002, Alam *et al.*, 2003b, Alam *et al.* 2006, Zhang *et al.* 2006, Kuo *et al.*, 2007). Employing hotwire and loadcell measurement techniques, Alam and Zhou (2008) at $Re = 2.72 \times 10^4$ studied the flow around the downstream cylinder for L/d = 5.5 when d/D was varied from 0.24 to 1.0. They identified two frequencies in the wake of the downstream cylinder, one associated with the downstream cylinder shedding and the other with the upstream cylinder. With decreasing d/D, the $\bar{C}_D$ increases because of a larger dynamic pressure between

*Corresponding author, Professor,
E-mail: alamm28@yahoo.com; alam@hit.edu.cn

ISSN: 1226-6116 (Print), 1598-6225 (Online)

the cylinders, and fluctuating lift and drag decline because of the impaired strength of vortices from the upstream cylinder. The detailed information on the effect of the gap vortex impingement on the pressure on the downstream cylinder surface and wake structure (e.g., formation length, wake width, etc) was missing in their study. Furthermore, they did not measure the forces on the upstream cylinder while a curiosity arises about how the forces on the upstream change with *d/D* decreasing from 1.0 to 0.24.

Gao *et al.* (2014) at $1.2 \times 10^3 \leq Re \leq 4.8 \times 10^3$ conducted particle image velocimetry (PIV) experiments in a water channel for a fixed *d/D* = 0.66 with *L/d* = 0.7, 1.9, 3.1 and 4.5. Three flow patterns identified are reattachment flow (*L/d* = 0.7 and 1.9), bistable flow (*L/d* = 3.1), and coshedding flow (*L/d* = 4.5). Heat transfer characteristics of an isothermal cylinder submerged in the wake of another cylinder were studied by Mahir and Altaç (2017) for *d/D* = 0.3 to 2 and *L/d* = 1.5 to 5 at *Re* = 100 and 200. They identified four flow regimes i.e. overshoot flow, steady reattachment flow, front-side-reattachment flow, and coshedding flow. The boundaries between these flow regimes are dependent on *d/D* and *Re*. Recently, Zafar and Alam (2018) examined the characteristics of heat transfer from a cylinder placed in the wake of another for *d/D* = 0.15 - 1.0 at a fixed *L/d* = 5.5. The surface-averaged heat transfer increases and decreases with *d/D* decreasing from 1.0 to 0.4 and from 0.4 to 0.15, respectively. The increase in heat transfer results from an enhanced shear layer velocity, reduced wake-recirculation size, and increased recirculation strength. A novel tertiary frequency in heat transfer fluctuation is identified, attributed the change of the instantaneous phase lag between the primary and secondary vortex sheddings.

Obviously, the previous investigations have improved our understanding of the salient features of the flow around two tandem different diameter cylinders, there is still scope of further investigation to understand the effect of *d/D* on pressure and friction force distributions, wake width, formation length, forces, etc. The objective of the present work is thus to study the influence of *d/D* on wake structure around the two tandem cylinders, in terms of shedding frequencies, global fluid forces, surface pressure, skin friction forces, wake width, and formation length at *Re* = 200. The *d/D* is systematically varied as *d/D* = 0.24, 0.4, 0.6, 0.8 and 1.0 for *L/d* = 5.5.

2. Problem description

The problem considered in this investigation is shown in Fig. 1. Two circular cylinders of different diameters are placed in a tandem arrangement. The diameter *d* of the upstream cylinder is varied while the diameter *D* of the downstream cylinder is fixed for diameter ratios of *d/D* =1.0, 0.8, 0.6, 0.4, and 0.24. The spacing ratio *L/d* = 5.5 is constant, where *L* is the spacing between the center of the upstream cylinder to the front stagnation point of the downstream cylinder. Two coordinates systems (x', y') with the origin at the center of the upstream cylinder and (x, y) with the origin at the center of the downstream cylinder are deployed.

An incompressible fluid flow is assumed, and the Reynolds number is set as *Re* = 200 based on *D* and freestream velocity U_∞. A rectangular computational domain is used for the simulations where $X_u = 10D$ is the distance from the center of the upstream cylinder to the inflow boundary, $X_d = 25D$ is the distance from the center of the downstream to the outflow boundary, and H = 30*D* is the lateral distance between the upper and lower boundaries (Fig. 1). Various studies (Mittal *et al*. 2006, Prasanth and Mittal 2008, Qu *et al.* 2013, Zheng and Alam 2017) have shown that the effect of the blockage ratio *B* = *D*/H can be ignored if B < 5% for *Re* < 300. Taking this point into account, *B* = 1/30 = 3.3% is adopted in the present study.

3. Computational method and validation

The unsteady incompressible viscous fluid flow motion is governed by the non-dimensional mass conservation and Navier–Stokes equations written as follows.

Mass Conservation

$$\frac{\partial u^*}{\partial x^*} + \frac{\partial v^*}{\partial y^*} = 0 \tag{1}$$

Momentum Conservation

$$\frac{\partial u^*}{\partial t^*} + u^* \frac{\partial u^*}{\partial x^*} + v^* \frac{\partial u^*}{\partial y^*} = -\frac{\partial p^*}{\partial x^*} + \frac{1}{Re}\left(\frac{\partial^2 u^*}{\partial x^{*2}} + \frac{\partial^2 u^*}{\partial y^{*2}}\right) \tag{2}$$

$$\frac{\partial v^*}{\partial t^*} + u^* \frac{\partial v^*}{\partial x^*} + v^* \frac{\partial v^*}{\partial y^*} = -\frac{\partial p^*}{\partial y^*} + \frac{1}{Re}\left(\frac{\partial^2 v^*}{\partial x^{*2}} + \frac{\partial^2 v^*}{\partial y^{*2}}\right) \tag{3}$$

The dimensionless variables are

$$x^* = \frac{x}{D},\quad y^* = \frac{y}{D},\quad u^* = \frac{u}{U_\infty},\quad v^* = \frac{v}{U_\infty},\quad p^* = \frac{p}{\rho U_\infty^2}$$

$$t^* = \frac{tU_\infty}{D}$$

Here *u* and *v* are the streamwise and normal components of the velocity, respectively, in the Cartesian coordinate system, *p* is the static pressure, and *t* is the time. The finite volume method in a commercial computational fluid dynamics package ANSYS FLUENT was used for the solution of these equations on hexahedral grids. Semi-Implicit Method for Pressure-Linked Equations (SIMPLE) scheme was adopted for the velocity pressure coupling while the second-order upwind differencing and second-order central differencing schemes for the discretization of convective and diffusive terms, respectively. The temporal discretization for the transient solution was performed using the second-order backward Euler scheme.

The hexahedral non-uniform grid system was employed. A higher grid density was rendered near the surfaces of the cylinders to resolve the viscous boundary layer. Therefore, an O-grid was generated in the vicinity of cylinders, with the first grid cell height of 0.00375*D*, consistent with the viscous length scale (Schlichting and Gersten 2003). Fig. 2 shows grids around the two cylinders. The O-grid system had 300 evenly spaced grid points in the circumferential

direction and 75 grid points in the radial direction. The following boundary conditions were enforced at different surfaces.

$u^* = 0,\ v^* = 0$ at the surface of cylinder,

$u^* = 1,\ v^* = 0$ at the inlet,

$\frac{\partial u^*}{\partial y^*} = 0,\ v^* = 0$ at the lateral sides, and

$\frac{\partial u^*}{\partial x^*} = 0,\ \frac{\partial v^*}{\partial x^*} = 0$ at the outlet.

The flow is initialized at $t^* = 0$ with inflow velocities $u^* = 1,\ v^* = 0$.

3.1 Aerodynamics parameter definitions

The following non-dimensional flow parameters related to fluid dynamics are computed. Drag coefficient $C_D = 2F_x/(\rho U_\infty^2 D)$, where F_x is the total drag force in the x direction, including pressure and friction forces. Lift coefficient $C_L = 2F_y/(\rho U_\infty^2 D)$, where F_y is the total force in the y direction. Pressure coefficient $C_p = 2(p - p_\infty)/(\rho U_\infty^2)$, where p_∞ is the freestream pressure. Skin friction coefficient $C_f = 2\tau/(\rho U_\infty^2)$, where τ is the wall shear stress. Fluctuating lift and drag coefficients $C_{Lf} = 2F_{y,rms}/(\rho U_\infty^2 D)$ and $C_{Df} = 2F_{x,rms}/(\rho U_\infty^2 D)$, where $F_{y,rms}$ and $F_{x,rms}$ are the root-mean-square (r.m.s.) of lift and drag forces, respectively. Strouhal number $St = f_s D/U_\infty$, where f_s is the vortex shedding frequency obtained from the power spectrum of fluctuating lift force.

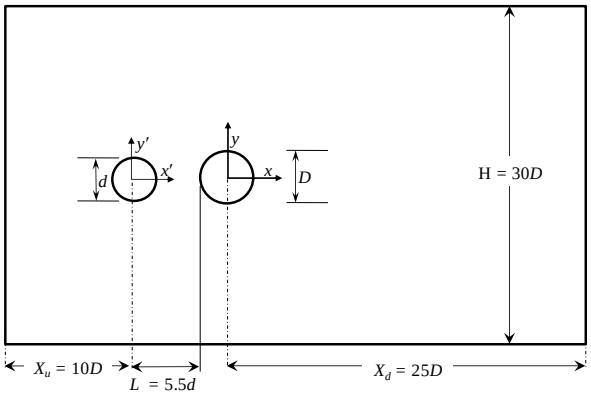

Fig. 1 Computational domain, definitions of symbols and arrangement of two cylinders

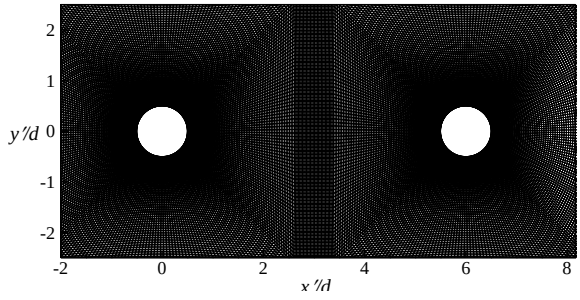

Fig. 2 Zoomed-in view of grids around the two cylinders

Time-mean drag coefficient ($\bar{C}_D$), time-mean friction force coefficient ($\bar{C}_f$), time-mean pressure coefficient ($\bar{C}_p$), fluctuating lift coefficient (C_{Lf}) and fluctuating drag coefficient (C_{Df}) are computed for more than 200 vortex shedding cycles after the computation is converged.

3.2 Grid validation study

Three different grid systems were tested first in order to decide the grid resolution. Grid1 consisted of 33934 nodes while grid2 and grid3 of 2×grid1 and 3×grid1, respectively, for a single cylinder (Table 1). A summary of the global aerodynamic coefficients (St, $\bar{C}_D$, and C_{Lf}) is given in table 1 for two different time steps. At time step $\Delta t^* = 0.0912$, the maximum variation in St, $\bar{C}_D$, and C_{Lf} is < 2.8% (for C_{Lf}) between grid1 and grid2, and < 3.3% (for C_{Lf}) between grid2 and grid3. On the other hand, at time step $\Delta t^* = 0.0182$, the maximum difference is < 1.03% (for St) between grid1 and grid2 and < 1.04% (for C_{Lf}) between grid2 and grid3. Grid2 and $\Delta t^* = 0.0182$ were, therefore, chosen. The effects of upstream and downstream boundaries on flow parameters were examined for grid 2. Two additional cases (cases 2 and 3) are considered as to grid2 (reference case, $X_u = 10D$, $X_d = 25D$) as shown in Table 2, where X_u is doubled (= 20D) in case 2 and X_d is doubled (= 50D) in case 3. The results obtained for cases 2 and 3 accord well those for the reference case, the deviation being less than 0.6% and 0.4%, respectively.

Table 1 Grid and time step independence test for a single cylinder at Re = 200

Grid	Nodes	$\Delta t^* = 0.0912$		
		St	$\bar{C}_D$	C_{Lf}
Grid1	33934	0.194	1.361	0.480
Grid2	2×Grid1	0.196	1.360	0.467
Grid3	3×Grid1	0.193	1.347	0.452
Grid	Nodes	$\Delta t^* = 0.0182$		
		St	$\bar{C}_D$	C_{Lf}
Grid1	33934	0.195	1.367	0.485
Grid2	2×Grid1	0.197	1.362	0.487
Grid3	3×Grid1	0.197	1.361	0.482

Table 2 Effects of upstream and downstream boundary locations on global parameters for a single cylinder at Re = 200

Case	Description	St	$\bar{C}_D$	C_{Lf}
1	Reference(grid2) ($X_u = 10D$, $X_d = 25D$)	0.197	1.362	0.487
2	X_u double ($X_u = 20D$, $X_d = 25D$)	0.196	1.358	0.484
3	X_d double ($X_d = 10D$, $X_d = 50D$)	0.197	1.363	0.489

Table 3 Comparison of global flow parameters for a single cylinder at Re = 200

	St	$\bar{C}_D$	C_{Lf}	$-\bar{C}_{pb}$
Present	0.197	1.362	0.487	0.958
Liu *et al.* (1998)	0.192	1.31 ± 0.049	0.487	0.956
Chen *et al.* (1999)	0.197	1.33 ± 0.049	0.509	–
Meneghini *et al.* (2001)	0.196	1.3	0.495	–
Linnick and Fasel (2005)	0.197	1.34 ± 0.04	0.487	–
Ding *et al.* (2007)	0.196	1.348 ± 0.05	0.466	–
Mahír and Altaç (2008)	0.192	1.37 ± 0.048	0.493	–
Qu *et al.* (2013)	0.196	1.316	0.467	0.966
Ma and Kuo (2016)	0.197	1.35 ± 0.048	0.487	0.971
Alam (2016)	0.195	1.40	0.488	–
Experiment				
Roshko (1954)	0.18	–	–	–
Williamson (1988)	0.197	–	–	0.96
Norberg (2003)	0.197	–	0.495	–

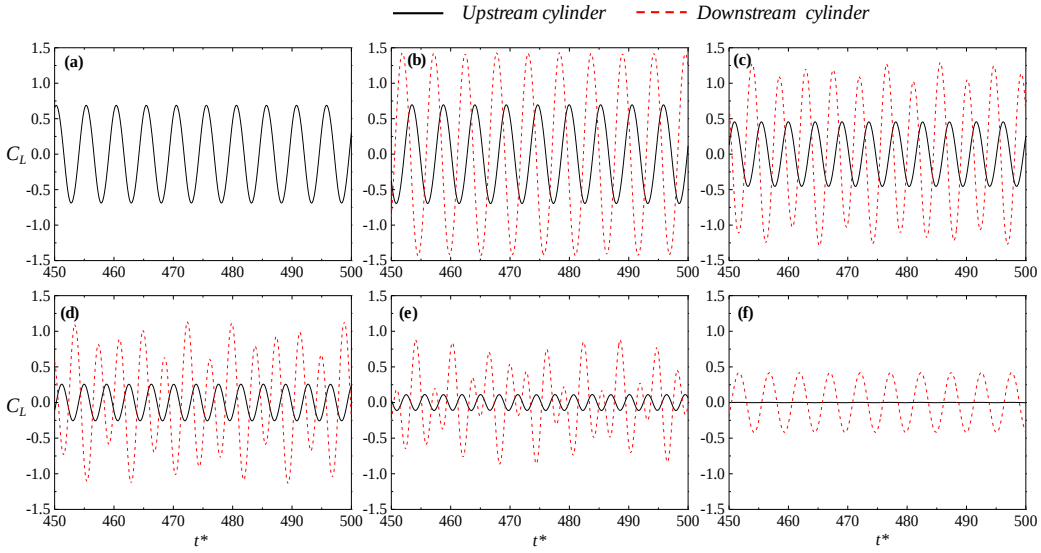

Fig. 3 Time histories of lift coefficient C_L of (a) single cylinder, (b) d/D = 1.0, (c) d/D = 0.8, (d) d/D = 0.6, (e) d/D = 0.4, and (f) d/D = 0.24

In view of computational cost and numerical accuracy, grid2 with X_u = 10D and X_d = 25D was adopted for the extensive simulation. The results (St, $\bar{C}_D$, C_{Lf}, time-mean base pressure coefficient $\bar{C}_{pb}$) are validated with those available in the literature in Table 3, showing a good agreement between the present and literature results.

4. Results and discussion

4.1 Lift force histories and flow structures

Fig. 3 shows time histories of C_L of the upstream and downstream cylinders for d/D = 1.0, 0.8, 0.6, 0.4, and 0.24. A single cylinder C_L is also included for a comparison purpose. Time histories are plotted for a span of non-dimensional time t^* = 450 to 500 beyond the transient state of the computation. It can be observed in Figs. 3(a) and 3(b) that the maximum amplitudes of C_L for the single and upstream cylinders (d/D = 1.0) are $C_{L,\max}$= 0.68 and 0.69, respectively. This implies that the vortices generated from the upstream cylinder are comparable to those from a single cylinder. On the other hand, the $C_{L,\max}$ for the downstream cylinder is 1.43, almost double of that for the upstream or single cylinder.

The upstream-cylinder generated vortices impinging on the downstream cylinder engender such a large $C_{L,\max}$ on the downstream cylinder. The periodical variation in C_L is regular, $C_{L,\max}$ being independent of time, for the two cylinders (d/D = 1.0) and the single cylinder. For d/D = 0.8 (Fig. 3(c)), the upstream cylinder $C_{L,\max}$ = 0.45, about 34% smaller than that for d/D = 1.0. The downstream cylinder C_L variation is not regular but quasi-regular, $C_{L,\max}$ varying between 1.27 and 1.02. While the upstream cylinder $C_{L,\max}$ monotonically decreases from d/D = 1.0 to 0.4 (Figs. 3(b)-3(e)), the regularity of C_L variation deteriorates for the

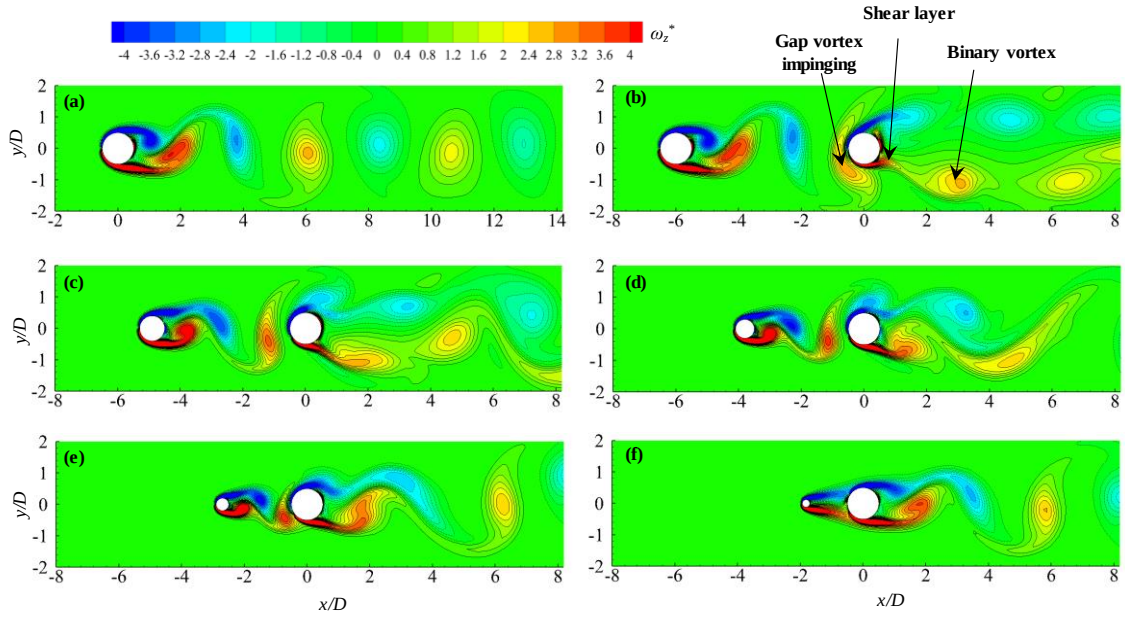

Fig. 4 Contours of instantaneous vorticity $\omega_z^* = \omega_z \times D/U_\infty$ for (a) single cylinder, (b) d/D = 1.0, (c) d/D = 0.8, (d) d/D = 0.6, (e) d/D = 0.4, and (f) d/D = 0.24. Solid and dashed lines represent positive and negative vorticities, respectively

downstream cylinder as d/D decreases from 0.8 to 0.4 (Figs. 3(c)-3(e)). It is noted that $C_{L,\max} \approx 0$ for the upstream cylinder at d/D = 0.24 (Fig. 3(f)), indicating no vortex shedding from the upstream cylinder. The downstream cylinder C_L, however, again becomes regular with $C_{L,\max}$ = 0.42. The observation is rather different from that at high Re = 2.72×10^4 by Alam and Zhou (2008), where they observed vortex shedding from the upstream cylinder for d/D = 0.24.The shear layers from the upstream cylinder reattach on the downstream cylinder, and the flow in the gap is quasi-steady. It can be pointed out that the flow past a single isolated cylinder is steady for Re < 50 (Berger and Wille 1972, Gresho *et al.* 1984). At d/D = 0.24, the effective Reynolds number Re_d (based on d) for the upstream cylinder is about 48. This is a reason why there is no vortex shedding in the gap for d/D = 0.24. Qin *et al.* (2017) and Wang *et al.* (2017) at Re = $4.8\times10^3 - 5.5\times10^4$ obtained that the critical spacing is longer for a smaller d/D, increasing from 3.0 to 6.5 as d/D decreases from 1.0 to 0.2.

Flow structures in the gap and wake are illustrated by instantaneous vorticity $\omega_z^* = \omega_z \times D/U_\infty$ contours for d/D = 1.0, 0.8, 0.6, 0.4, 0.24 and single cylinder in Fig. 4. For the single cylinder, a single vortex street is well established, symmetric about the wake centerline (Fig. 4(a)), and two single vortices shed in one shedding cycle (Fig. 3(a)), one negative vortex from the upper surface and one positive vortex from the lower surface (Fig. 4(a)). For the two-cylinder case (Figs. 4(b)-4(e)), the gap vortices generated by the upstream cylinder impinge on the downstream cylinder surface, followed by interactions with the shear layers of the downstream cylinder, which leads to shedding of binary vortices from the downstream cylinder (Fig. 4(b)). The upstream cylinder sheds vortices in the gap for $0.4 \le d/D \le 1.0$ in a similar fashion to the single cylinder. As d/D is decreased from 1.0 to 0.4, the vortices in the gap become smaller in size, and a low-frequency modulation of the downstream-cylinder wake is found to shift upstream. The detailed physics of the modulation has been explained in Zafar and Alam (2018). For d/D = 0.24, the shear layers separated from upstream cylinder reattach on the front surface of the downstream cylinder, and the flow in the gap is quasi-steady (Fig. 4(f)), while the vortex shedding occurs from the downstream cylinder only. The nature, formation, and size of vortices in the wake are quite comparable with those in the single-cylinder wake; the C_L amplitudes are however different from each other due to the placement of the small upstream cylinder.

4.2 Global fluid forces

The dependence of $\bar{C}_D$, C_{Df}, and C_{Lf} on d/D is presented in Fig. 5, where the subscripts 1, 2 and 0 in the figure stand for the upstream, downstream and single cylinders, respectively. Note that all the force coefficients are normalized based on D. As seen in Fig. 5(a), the upstream cylinder experiences maximum $\bar{C}_{D1}$ for d/D = 1.0, albeit less than the single cylinder $\bar{C}_{D0}$, due to an interference effect of the downstream cylinder. With d/D decreasing from 1.0 to 0.24, $\bar{C}_{D1}$ declines and $\bar{C}_{D2}$ boosts. The expected decline of $\bar{C}_{D1}$ is attributed to the reductions of the vortex size as well as of the upstream cylinder size. On the other hand, the enhancement of $\bar{C}_{D2}$ with decreasing d/D results from the reduced shielding effect by the upstream cylinder. Further explanations behind the decline and boost will be given later with the aid of pressure distributions and skin friction forces on the cylinder surfaces.

Interestingly, $\bar{C}_{D2} < \bar{C}_{D1} < \bar{C}_{D0}$ for $d/D \ge 0.6$ while $\bar{C}_{D1} < \bar{C}_{D2} < \bar{C}_{D0}$ for $d/D < 0.6$. It is worthy of examining how the total drag force coefficient $\bar{C}_{Dtotal}$ (= $\bar{C}_{D1}+\bar{C}_{D2}$) varies with d/D. Fig. 5(b) depicts the variation in $\bar{C}_{Dtotal}$ with d/D.

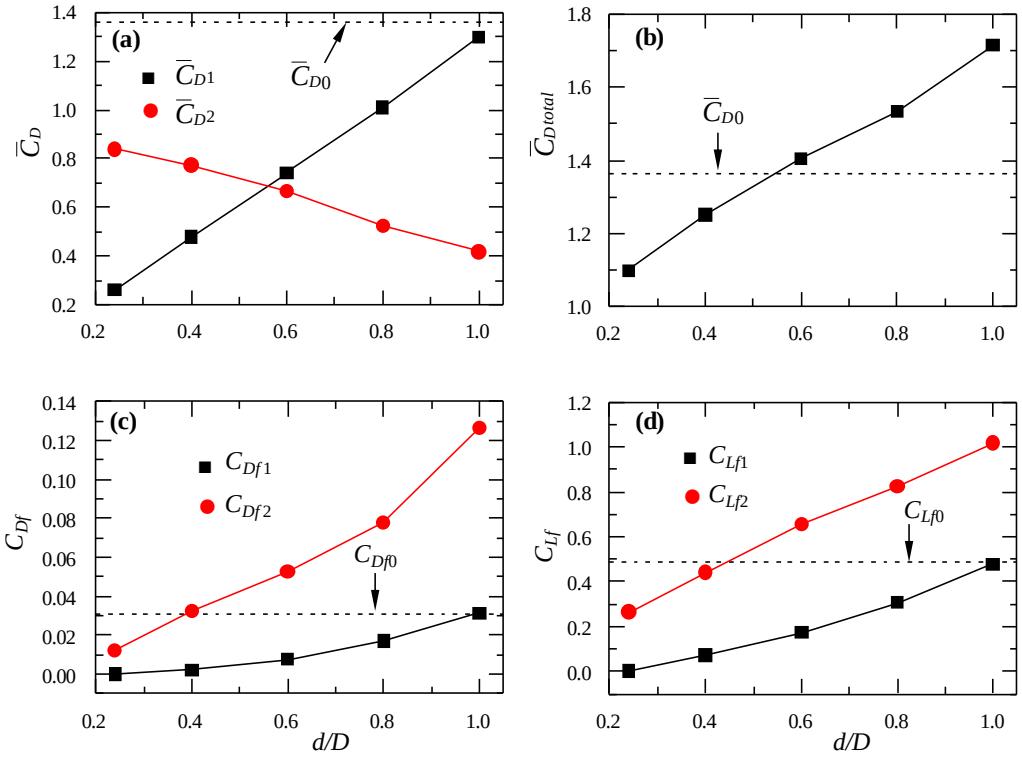

Fig. 5 Dependence on d/D of (a) time-mean drag coefficient ($\overline{C}_D$), (b) total time-mean drag coefficient ($\overline{C}_{Dtotal}$), (c) fluctuating drag coefficient (C_{Df}), and (d) fluctuating lift coefficient (C_{Lf}). The subscripts 1, 2 and 0 stand for the upstream, downstream and single cylinders, respectively

Interestingly, although $\overline{C}_{D2}$ boosts with decreasing d/D, the $\overline{C}_{Dtotal}$ dwindles with decreasing d/D. The $\overline{C}_{Dtotal} < \overline{C}_{D0}$ and $> \overline{C}_{D0}$ for d/D < 0.58 and > 0.58, respectively, which explains why a smaller cylinder is used to control the flow over a large cylinder. This information may be very useful in engineering practice where different-sized structures are designed for coshedding flow regimes.

The C_{Df} behaves differently from the $\overline{C}_D$, where C_{Df1} and C_{Df2} both follow the same trend, declining with decreasing d/D (Fig. 5(c)). While $C_{Df2} > C_{Df1}$ and $C_{Df1} < C_{Df0}$ for the entire d/D range, $C_{Df2} > C_{Df0}$ for $d/D > 0.4$ only. The difference between C_{Df2} and C_{Df1} is larger at a larger d/D because of a stronger impingement of alternating large-sized vortices on the downstream cylinder. As to C_{Lf}, similar characteristics of C_{Lf2} and C_{Lf1} are discernible to those of C_{Df2} and C_{Df1} (Figs. 5(c) and 5(d)) That is, the vortex impingement plays the same role in C_{Lf2} as in C_{Df2}. Again, the decline of C_{Lf2} is connected to smaller d accompanied by smaller vortex size.

4.3 Pressure and shear forces

The drag force is composed of the pressure and shear forces acting on the cylinder surface. The pressure drag results from the variation in the pressure around the cylinder while tangential shear stresses acting on the surface produce the skin friction drag. Fig. 6(a) presents distributions of time-mean pressure coefficient $\overline{C}_p$ along the surface of the downstream cylinder for different d/D. It is observed that $\overline{C}_p$ at the front stagnation point (θ° = 0) is 0.028, 0.155, 0.235, 0.214, and 0.08 for d/D = 1.0, 0.8, 0.6, 0.4, and 0.24, respectively, increasing for $0.6 \leq d/D \leq 1.0$ and then decreasing for $d/D < 0.6$. It is less for d/D = 1.0, owing to a wider wake by the upstream cylinder (Fig. 4(b)); more information will be rendered later. It is again much less for d/D = 0.24 because of the symmetric standing recirculation at the front of the downstream cylinder (Fig. 4(f)). The $\overline{C}_p$ for $0.4 \leq d/D \leq 1.0$ decreases from θ = 0° to 87-90° (depending on d/D) and then increases. On the other hand, that for d/D = 0.24 increases up to θ = 33° which is followed by a decrease for θ = 33° to 90° and an increase for θ > 90°. The minimum pressure coefficient $\overline{C}_{p,\min}$ occurs at 90°, 88.40°, 87.61°, 87.58° and 87.56° for d/D = 1.0, 0.8, 0.6, 0.4, and 0.24, respectively. With decreasing d/D, the point of $\overline{C}_{p,\min}$ postpones. It is interesting to note that the base pressure coefficient $\overline{C}_{pb}$ (at θ = 180°) = -0.418, -0.462, -0.545, -0.620, and -0.675 for d/D = 1.0, 0.8, 0.6, 0.4, and 0.24, respectively, the magnitude of $\overline{C}_{pb}$ increasing. The observation indicates that the pressure difference between the front and back surfaces enhances with decreasing d/D, explaining why $\overline{C}_{D2}$ augments with d/D decreasing (Fig. 5(a)). The reason behind the $\overline{C}_{pb}$ magnitude increasing will be given later.

Skin friction coefficient $\overline{C}_f$ is considered as an important parameter, determining the flow separation and heat transfer from the surface. It is well-known that the attached and separated flow regions corresponds $\overline{C}_f > 0$ and $\overline{C}_f < 0$, respectively, with $\overline{C}_f = 0$ at the separation point. Fig. 6(b)

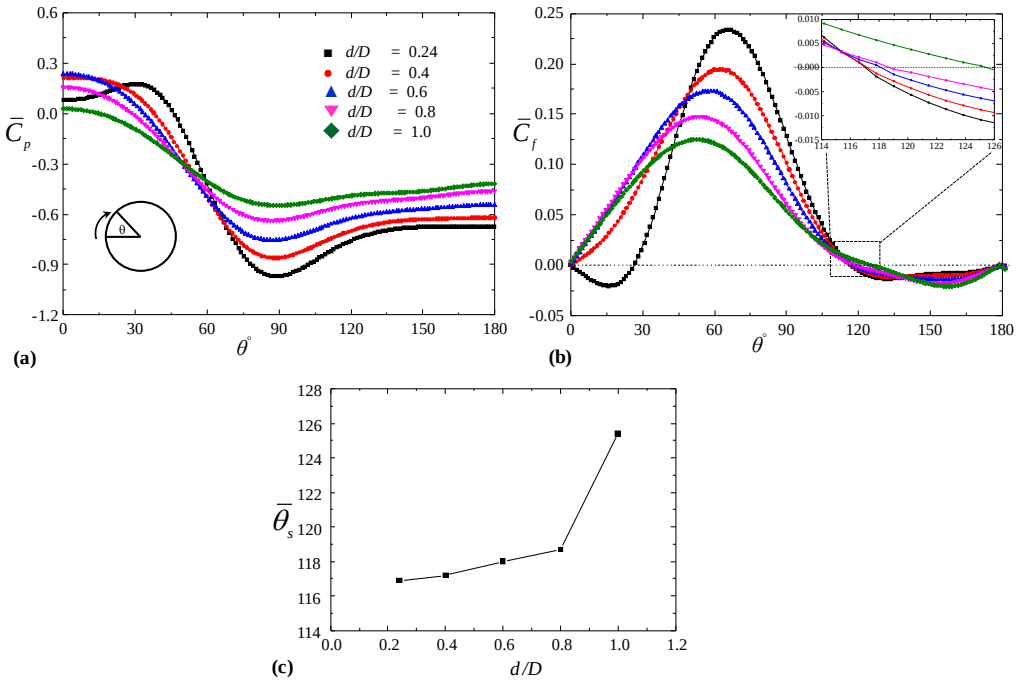

Fig. 6 (a) Time-mean pressure coefficient $\bar{C}_p$ along cylinder surface, (b) time-mean friction coefficient $\bar{C}_f$ along cylinder surface, and (c) time-mean separation angle $\bar{\theta}_s$ variation with *d/D*

shows $\bar{C}_f$ distributions on the surface of the downstream cylinder. For *d/D* = 1.0, the $\bar{C}_f$ escalates for θ < 50°, as the flow in the boundary layer accelerates due to a favorable pressure gradient. The trends of $\bar{C}_f$ for *d/D* ≥ 0.4 are the same, albeit the peak magnitude grows with a decrease in *d/D*. For *d/D* = 0.24 where the shear layers from the upstream cylinder reattach on the downstream cylinder, $\bar{C}_f$ < 0 for θ < 27° indicating the reattachment of the upstream-cylinder-generated shear layer at θ = 27°. A large favorable pressure gradient at 27° < θ < 66° results in an accelerated flow, hence causing a rapid growth of $\bar{C}_f$. As already stated, $\bar{C}_D$ increases with decreasing *d/D*, contributed by $\bar{C}_f$ increasing. The increase in pressure for 85°-90° < θ < 130°corresponds to decreasing $\bar{C}_f$ with θ. The separation point of the flow where $\bar{C}_f$ = 0 (widely accepted definition of the boundary layer separation) occurs at 117 < θ < 126° depending on *d*/D. Fig. 6(c) shows the variation of time-mean separation point $\bar{\theta}_s$ with *d/D* while the inset in Fig. 6b shows the zoomed-in view of $\bar{C}_f$ used for estimating $\bar{\theta}_s$. The $\bar{\theta}_s$ sharply drops from *d/D* = 1.0 to 0.8, followed by a linear decrease for *d/D* ≤ 0.8.

4.4 Correspondence between drag enhancement and flow structure

As observed earlier, $\bar{C}_{D2}$ enhances with decreasing *d/D*. Here we would try to correlate this enhancement with the flow structure. Vortex formation length L_F and wake width W are two important parameters describing the characteristics of vortex formation and vortex street. They are obtained from contour plots of fluctuating streamwise velocity $u^*_{rms} = u_{rms}/U_\infty$ as shown in Fig. 7(a). The streamwise distance from the cylinder center to the maximum u^*_{rms} point is defined as the vortex formation length L_F (Bloor 1964, Gerrard 1966, Alam and Zhou 2007). On the other hand, W is defined as the transverse separation between the two maxima of u^*_{rms} (Alam *et al.* 2011, Bai and Alam 2018). Fig. 7(c) shows the dependence on *d/D* of L_{F2}/D (left axis) and $-\bar{C}_{pb2}$ (right axis) for the downstream cylinder. As seen, the L_{F2}/D has a strong link with $-\bar{C}_{pb2}$, when *d/D* decreases from 1.0 to 0.24, $-\bar{C}_{pb2}$ increases from 0.418 to 0.675 and L_{F2}/D shrinks from 9.0 to 1.63. That is, $-\bar{C}_{pb}$ and L_{F2}/D are inversely related, albeit not straightforward. The wake width W_1/D of the upstream cylinder has a correspondence with the front stagnation pressure coefficient $\bar{C}_{ps2}$ of the downstream cylinder (Fig. 7(d)). With decreasing *d/D*, W_1/D shrinks from 0.90 to 0.54 for 0.4 ≤ *d/D* ≤ 1.0 which is accompanied by $\bar{C}_{ps2}$ increasing from 0.028 to 0.235 for 0.6 ≤ *d/D* ≤ 1.0 and decreasing for *d/D* ≤ 0.4. For *d/D* = 0.24, as the vortex shedding did not take place in the gap between the cylinders, there is no wake width. Thus, both L_{F2} and W_1 can determine the $\bar{C}_{D2}$. In general, a shorter formation length corresponds to a higher magnitude of the base pressure, hence a higher drag. On the other hand, a smaller W_1 may give rise to a higher $\bar{C}_{ps2}$, hence a higher $\bar{C}_{D2}$. It is interesting to note that increasing $\bar{C}_{ps2}$ for 1.0 ≥ *d/D* ≥ 0.6, complemented by the impaired W_1, buoys up $\bar{C}_{Dtotal} > \bar{C}_{D0}$, while the decreasing $\bar{C}_{ps2}$ for *d/D* < 0.6 makes $\bar{C}_{Dtotal} < \bar{C}_{D0}$ (Fig. 5(b)). The maximum time-mean streamwise velocity $\bar{u}^*_{\max} = \bar{u}/U_\infty$ around the downstream cylinder (Fig. 7(b)), representing shear layer velocity, may also be connected to $\bar{C}_{D2}$. Roshko (1954) obtained shear layer velocity u_s from empirical

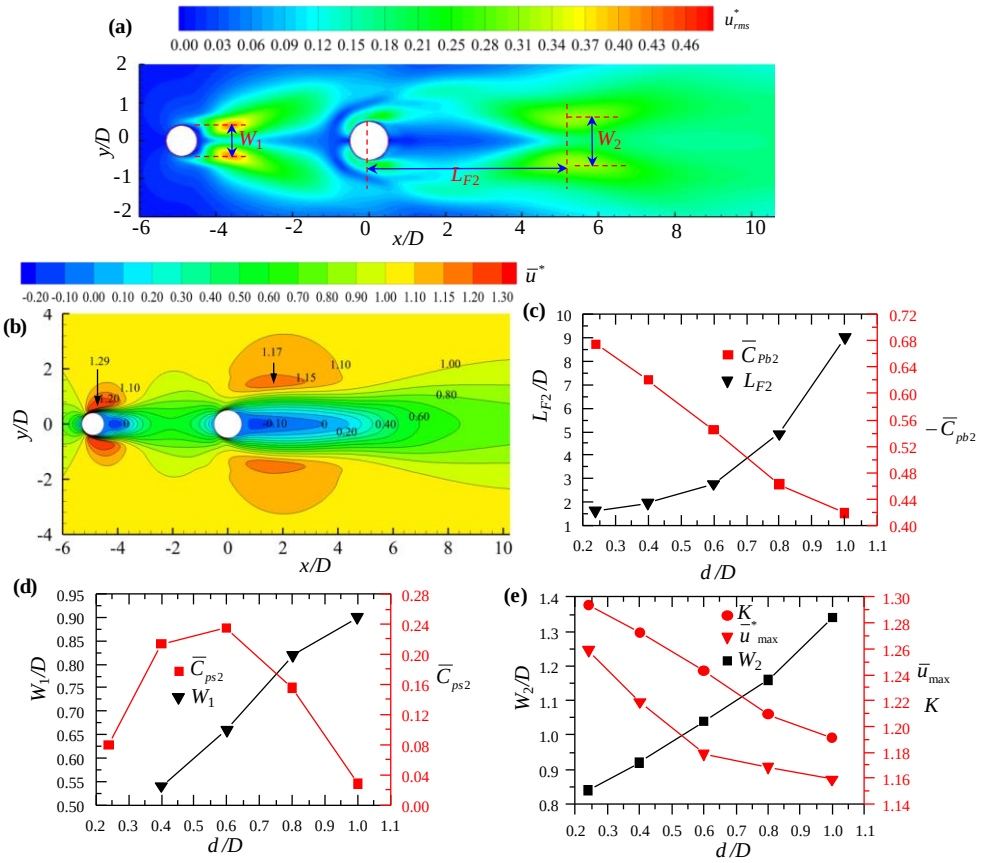

Fig. 7 Contour plots, for d/D = 0.8, of (a) fluctuating streamwise velocity u^*_{rms} to illustrate the definitions of vortex formation length and wake width, (b) time-mean streamwise velocity $\bar{u}^*$ to illustrate the maximum velocity in shear layer, (c) dependence on d/D of vortex formation length L_{F2}/D and base pressure coefficient $\bar{C}_{pb2}$ of the downstream cylinder, (d) the relationship between the wake width W_1/D of the upstream cylinder and the front-stagnation pressure coefficient $\bar{C}_{ps2}$ of the downstream cylinder, and (e) dependence on d/D of the downstream-cylinder wake width W_2/D, shear layer velocity parameter (K), and maximum shear layer velocity $\bar{u}^*_{max}$

the relationships between W_2, $\bar{u}^*_{\max}$ and K as a function of d/D. The relationship signifies that one can measure shear layer velocity by measuring $\bar{C}_{pb}$. The difference between K and $\bar{u}^*_{max}$ is less than 5%, with the maximum difference occurring at d/D = 0.6. The W_2 and $\bar{u}^*_{max}$ are inversely related, decreasing and growing with d/D. The variation in $\bar{C}_{D2}$ follows that in $\bar{u}^*_{\max}$ while the relationship between $\bar{C}_{D2}$ and W_2 is opposite (Alam and Zhou 2008)

5. Conclusions

Numerical simulations have been conducted to study the fluid flow around two tandem circular cylinders of diameter ratios d/D = 1.0, 0.8, 0.6, 0.4 and 0.24 at L/d = 5.5 for Re = 200. The main conclusions are summarized as follows.

For $d/D \geq 0.4$, the upstream cylinder sheds vortices in the gap and the downstream cylinder in the wake. The wake vortices are binary coupled by pairing up with the gap vortices. On the other hand, at d/D = 0.24, there is no vortex shedding from the upstream cylinder in the gap due to the effective Re falling below 48, a quasi-steady flow prevailing in the gap with the upstream-cylinder shear layers reattaching on the downstream cylinder.

Fluid forces $\bar{C}_D$, C_{Df}, C_{Lf}, and $\bar{C}_{Dtotal}$ show strong dependence with d/D. With d/D decreasing from 1.0 to 0.24, $\bar{C}_{D1}$ declines and $\bar{C}_{D2}$ boosts. The expected decline of $\bar{C}_{D1}$ is attributed to the reduction in the vortex size as well as of the upstream cylinder size. On the other hand, the enhancement of $\bar{C}_{D2}$ with decreasing d/D results from the reduced shielding effect by the upstream cylinder. The $\bar{C}_{Dtotal}$ also decreases with decreasing d/D, following $\bar{C}_{D1}$. C_{Df} and C_{Lf} both show declining trends with decreasing d/D.

An in-depth understanding of the flow as well as $\bar{C}_{D2}$ enhancement with d/D decreasing is obtained through measurements of $\bar{C}_p$, $\bar{C}_{pb2}$, $\bar{C}_{ps2}$, $\bar{C}_f$, $\bar{\theta}_s$, $\bar{u}^*_{max}$, K, W_1, W_2 and L_{f2}. With decreasing d/D, (i) an increased difference between $-\bar{C}_{pb2}$ and $\bar{C}_{ps2}$ leads to the enhanced $\bar{C}_{D2}$, mostly contributed by a rapid increase in $-\bar{C}_{Pb2}$, (ii) $\bar{C}_f$ on the side surface increasing, playing a role in the enhancement

of $\overline{C}_{D2}$, (iii) $\overline{\theta}_s$ shifts toward the front stagnation point, again contributing to $\overline{C}_{D2}$ enhancement, (iv) L_{F2} and W_2 decline, inversely related to $\overline{C}_{D2}$, and (v) $\overline{u}^*_{max}$ and K both augment, following $\overline{C}_{D2}$.

Acknowledgements

ALAM wishes to acknowledge the support given by the National Natural Science Foundation of China through Grants 11672096 and 91752112 and by Research Grant Council of Shenzhen Government through grant JCYJ20170811152808282.

References

Alam, M.M. (2014), "The aerodynamics of a cylinder submerged in the wake of another", *J. Fluid. Struct.*, **51**, 393-400. https://doi.org/10.1016/j.jfluidstructs.2014.08.003.

Alam, M.M. (2014), "The aerodynamics of a cylinder submerged in the wake of another". *J. Fluid. Struct.*, **51**, 393-400. https://doi.org/10.1016/j.jfluidstructs.2014.08.003.

Alam, M.M. (2016), "Lift forces induced by phase lag between the vortex sheddings from two tandem bluff bodies", *J. Fluid. Struct.*, **65**, 217-237. https://doi.org/10.1016/j.jfluidstructs.2016.05.008.

Alam, M.M., Moriya, M., Takai, K. and Sakamoto, H. (2002), "Suppression of fluid forces acting on two square prisms in a tandem arrangement by passive control of flow", *J. Fluid. Struct.*, **16**, 1073-1092. https://doi.org/10.1006/jfls.2002.0458.

Alam, M.M., Moriya, M., Takai, K. and Sakamoto, H. (2003a), "Fluctuating fluid forces acting on two circular cylinders in a tandem arrangement at a subcritical Reynolds number", *J. Wind Eng. Ind. Aerod.*, **91**(1-2), 139-154. https://doi.org/10.1016/S0167-6105(02)00341-0.

Alam, M.M., Sakamoto, H. and Moriya, M. (2003b), "Reduction of fluid forces acting on a single circular cylinder and two circular cylinders by using tripping rods", *J. Fluid. Struct.*, **18**(3-4), 347-366. https://doi.org/10.1016/j.jfluidstructs.2003.07.011.

Alam, M.M., Sakamoto, H. and Zhou, Y. (2006), "Effect of a T-shaped plate on reduction in fluid forces on two tandem cylinders in a cross-flow", *J. Wind Eng. Ind. Aerod.*, **94**(7), 525-551. https://doi.org/10.1016/j.jweia.2006.01.018.

Alam, M.M. and Zhou, Y. (2007), "Turbulent wake of an inclined cylinder with water running", *J. Fluid Mech.*, **589**, 261-303. https://doi.org/10.1017/S0022112007007720

Alam, M.M. and Zhou, Y. (2008), "Strouhal numbers, forces and flow structures around two tandem cylinders of different diameters", *J. Fluid. Struct.*, **24**(4), 505-526. https://doi.org/10.1016/j.jfluidstructs.2007.10.001.

Alam, M.M., Zhou, Y. and Wang, X.W. (2011), "The wake of two side-by-side square cylinders", *J. Fluid Mech.*, **669**, 432-471. https://doi.org/10.1017/S0022112010005288.

Bai, H. and Alam, M.M. (2018), "Dependence of square cylinder wake on Reynolds number", *Phys. Fluids*, **30**(1), https://doi.org/10.1063/1.4996945.

Berger, E. and Wille, R. (1972), "Periodic flow phenomena", *Annu. Rev. Fluid Mech.*, **4**, 313-340. https://doi.org/10.1146/annurev.fl.04.010172.001525.

Bloor, M.S. (1964), "The transition to turbulence in the wake of a circular cylinder", *J. Fluid Mech.*, **19**(2), 290-304. https://doi.org/10.1017/S0022112064000726.

Bouak, F. and Lemay, J. (1998), "Passive control of the aerodynamic forces acting on a circular cylinder", *Exp. Therm Fluid Sci.*, **16**(1-2), 112-121. https://doi.org/10.1016/S0894-1777(97)10010-3.

Chen, Y.N., Yang, S.C. and Yang, J.Y. (1999), "Implicit weighted essentially non-oscillatory schemes for the incompressible Navier–Stokes equations", *Int. J. Numer. Meth. Fl.*, **31**, 747-765. https://doi.org/10.1002/(SICI)1097-0363(19991030)31:4<747.

Ding, H., Shu, C., Yeo, K.S. and Xu, D. (2007), "Numerical simulation of flows around two circular cylinders by mesh-free least square-based finite difference methods", *Int. J. Numer. Meth. Fl.*, **53**(2), 305-332. https://doi.org/10.1002/fld.1281.

Gao, Y., Etienne, S., Wang, X. and Tan, S. (2014), "Experimental study on the flow around two tandem cylinders with unequal diameters", *J. Ocean Univ. China*, **13**(5), 761-770.

Gerrard, J.H. (1966), "The mechanics of the formation region of vortices behind bluff bodies", *J. Fluid Mech.*, **25**(2), 401-413. https://doi.org/10.1017/S0022112066001721.

Gresho, P.M., Chan, S.T., Lee, R.L. and Upson, C.D. (1984), "A modified finite element method for solving the time-dependent, incompressible Navier-Stokes equations. Part 2: Applications", *Int. J. Numer. Meth. Fl.*, **4**(7), 619-640. https://doi.org/10.1002/fld.1650040703.

Igarashi, T. (1982), "Characteristics of a flow around two circular cylinders of different diameters arranged in tandem". *Bulletin of JSME.*, **25**, 349-357. https://doi.org/10.1299/jsme1958.25.349.

Igarashi, T. (1997), "Drag reduction of a square prism by flow control using a small rod", *J. Wind Eng. Ind. Aerod.*, **69-71**, 141-153. https://doi.org/10.1016/S0167-6105(97)00150-5.

Kuo, C.H., Chiou, L.C. and Chen, C.C. (2007), "Wake flow pattern modified by small control cylinders at low Reynolds number", *J. Fluid. Struct.*, **23**(6), 938-956. https://doi.org/10.1016/j.jfluidstructs.2007.01.002.

Linnick, M.N. and Fasel, H.F. (2005), "A high-order immersed interface method for simulating unsteady incompressible flows on irregular domains", *J. Comput. Phys.*, **204**(1), 157-192. https://doi.org/10.1016/j.jcp.2004.09.017.

Liu, C., Zheng, X. and Sung, C.H. (1998), "Preconditioned multigrid methods for unsteady incompressible flows", *J. Comput. Phys.*, **139**(1), 35-57. https://doi.org/10.1006/jcph.1997.5859.

Ma, H.L. and Kuo, C.H. (2016), "Control of boundary layer flow and lock-on of wake behind a circular cylinder with a normal slit", *Eur. J. Mech. - B/Fluids*, **59**, 99-114. https://doi.org/10.1016/j.euromechflu.2016.05.001.

Mahir, N. and Altaç, Z. (2017), "Numerical investigation of flow and heat transfer characteristics of two tandem circular cylinders of different diameters", *Heat Transfer Eng.*, **38**, 1367-1381. https://doi.org/10.1080/01457632.2016.1255027.

Mahır, N. and Altaç, Z. (2008), "Numerical investigation of convective heat transfer in unsteady flow past two cylinders in tandem arrangements", *Int. J. Heat Fluid Fl*, **29**(5), 1309-1318. https://doi.org/10.1016/j.ijheatfluidflow.2008.05.001.

Meneghini, J.R., Saltara, F., Siqueira, C.L.R. and Ferrari, J.A. (2001), "Numerical simulation of flow interference between two circular cylinders in tandem and side-by-side arrangements", *J. Fluid. Struct.*, **15**(2), 327-350.

Mittal, S., Prakash Singh, S., Kumar, B. and Kumar, R. (2006), "Flow past bluff bodies: effect of blockage", *Int. J. Comp. Fluid Dyn.*, **20**, 163-173.

Norberg, C. (2003), "Fluctuating lift on a circular cylinder: review and new measurements", *J. Fluid. Struct.*, **17**(1), 57-96. https://doi.org/10.1016/S0889-9746(02)00099-3.

Prasad, A. and Williamson, C.H.K. (1997), "A method for the reduction of bluff body drag", *J. Wind Eng. Ind. Aerod.*, **69-71**, 155-167. https://doi.org/10.1016/S0167-6105(97)00151-7.

Prasanth, T.K. and Mittal, S. (2008), "Effect of blockage on free

vibration of a circular cylinder at low Re", *Int. J. Numer. Meth. Fl.*, **58**(10), 1063-1080. https://doi.org/10.1002/fld.1771.

Qin, B., Alam, M.M. and Zhou, Y. (2017), "Two tandem cylinders of different diameters in cross-flow: flow-induced vibration", *J. Fluid Mech.*, **829**, 621-658. https://doi.org/10.1017/jfm.2017.510.

Qu, L., Norberg, C., Davidson, L., Peng, S.H. and Wang, F. (2013), "Quantitative numerical analysis of flow past a circular cylinder at Reynolds number between 50 and 200", *J. Fluid. Struct.*, **39**, 347-370. https://doi.org/10.1016/j.jfluidstructs.2013.02.007.

Roshko, A. (1954), "On the drag and shedding frequency of bluff body", *NACA TN 3169*.

Sakamoto, H. and Haniu, H. (1988), "Effect of free-stream turbulence on characteristics of fluctuating forces acting on two square prisms in tandem arrangement", *J. Fluid. Eng.*, **110**(2), 140-146. doi:10.1115/1.3243526.

Sakamoto, H. and Haniu, H. (1994), "Optimum suppression of fluid forces acting on a circular cylinder", *J. Fluid. Eng.*, **116**(2), 221-227. doi:10.1115/1.2910258.

Schlichting, H. and Gersten, K. (2003), Boundary layer theory. Springer Berlin.

Tsutsui, T. and Igarashi, T. (2002), "Drag reduction of a circular cylinder in an air-stream", *J. Wind Eng. Ind. Aerod.*, **90**(4-5), 527-541. https://doi.org/10.1016/S0167-6105(01)00199-4.

Wang, L., Alam, M.M. and Zhou, Y. (2017), "Two tandem cylinders of different diameters in cross-flow: effect of an upstream cylinder on wake dynamics", *J. Fluid Mech.*, **836**, 5-42. https://doi.org/10.1017/jfm.2017.735.

Williamson, C.H.K. (1988), "Defining a universal and continuous Strouhal–Reynolds number relationship for the laminar vortex shedding of a circular cylinder", *Phys. Fluids*, **31**(10), 2742-2744. https://doi.org/10.1063/1.866978.

Zafar, F. and Alam, M.M. (2018), "A low Reynolds number flow and heat transfer topology of a cylinder in a wake", *Phys. Fluids*, **30**(8), https://doi.org/10.1063/1.5035105.

Zdravkovich, M.M. (1987), "The effects of interference between circular cylinders in cross flow", *J. Fluid. Struct.*, **1**(2), 239-261. https://doi.org/10.1016/S0889-9746(87)90355-0.

Zhang, P.F., Wang, J.J. and Huang, L.X. (2006), "Numerical simulation of flow around cylinder with an upstream rod in tandem at low Reynolds numbers", *Appl. Ocean Res.*, **28**(3), 183-192. https://doi.org/10.1016/j.apor.2006.08.003.

Zheng, Q. and Alam, M.M. (2017), "Intrinsic features of flow past three square prisms in side-by-side arrangement", *J. Fluid Mech.*, **826**, 996-1033. https://doi.org/10.1017/jfm.2017.378